

# Journal of Materials Chemistry A

Materials for energy and sustainability

Accepted Manuscript

This article can be cited before page numbers have been issued, to do this please use: J. Saha, T. K. Sahu, G. Salazar-Alvarez and M. Johnsson, *J. Mater. Chem. A*, 2026, DOI: 10.1039/D6TA00538A.



This is an Accepted Manuscript, which has been through the Royal Society of Chemistry peer review process and has been accepted for publication.

Accepted Manuscripts are published online shortly after acceptance, before technical editing, formatting and proof reading. Using this free service, authors can make their results available to the community, in citable form, before we publish the edited article. We will replace this Accepted Manuscript with the edited and formatted Advance Article as soon as it is available.

You can find more information about Accepted Manuscripts in the [Information for Authors](#).

Please note that technical editing may introduce minor changes to the text and/or graphics, which may alter content. The journal's standard [Terms & Conditions](#) and the [Ethical guidelines](#) still apply. In no event shall the Royal Society of Chemistry be held responsible for any errors or omissions in this Accepted Manuscript or any consequences arising from the use of any information it contains.

## ARTICLE

# Improved Electrocatalytic Oxidation of Artificial Seawater with an Applied Magnetic Field in a Forward Osmosis System

Jayeeta Saha,<sup>a</sup> Tushar Kanta Sahu,<sup>a</sup> German Salazar Alvarez,<sup>b</sup> Mats Johnsson<sup>\*a</sup>Received 00th January 20xx,  
Accepted 00th January 20xx

DOI: 10.1039/x0xx00000x

It is desirable to be able to use seawater directly for electrocatalytic splitting and hydrogen production. However, challenges such as electrode corrosion and chlorine gas evolution limit its practical application. In this study, a transition metal-based phosphide/phosphate (Ni–NiPO) catalyst on Ni foam was developed to improve charge transfer and suppress parasitic reactions. To improve stability and selectivity, a chloride ion-selective forward osmosis (FO) membrane was integrated into the system, which effectively minimised chlorine oxidation and corrosion. The FO membrane exhibited excellent stability (48 hours) and OER selectivity at pH 8. In addition, the application of a 100 mT magnetic field improved the OER kinetics, reducing the overpotential from 0.45 V to 0.31 V. It is shown that the combination of the Ni–NiPO catalyst, FO membrane and an applied magnetic field significantly improves the control of the OER reaction.

## Introduction

Rising concerns over environmental pollution and the global energy crisis have driven significant efforts toward developing clean and sustainable energy sources. Among these, hydrogen stands out as an abundant, renewable, and clean fuel, making it a highly promising alternative to fossil fuels. One of the most environmentally friendly and sustainable approaches for large-scale hydrogen production is electrocatalytic water splitting.<sup>1</sup> Achieving an efficient hydrogen evolution reaction (HER) and oxygen evolution reaction (OER) during electrocatalysis with a minimal overpotential is critical for advancing water-splitting technologies and reducing the amount of electricity consumed.<sup>2–5</sup> The energy required to conduct the four main stages (production, storage, safety, and utilisation) should be reduced for an economically viable hydrogen economy. Energy is needed for water purification and reaction activation for the production stage in the H<sub>2</sub> economy. The aim is to use substantially less energy for the overall process compared to the energy content of the produced H<sub>2</sub>. To stimulate the reaction, energy is needed in terms of overpotential, which can come either from conventional energy (fossil fuel) or alternative energy (wind, solar, hydro) for HER or OER.<sup>6</sup> Due to the slow kinetics, OER requires a large overpotential that significantly hinders the overall efficiency.<sup>1, 7</sup> So, to reduce the overpotential of the electrocatalytic reaction, modification of the electrocatalyst and electrolytes is often approached. While iridium- and ruthenium-based catalysts are currently considered the most effective and stable for OER, their large-

scale application is hindered by limited availability and high cost. Consequently, designing cost-effective, high-performance OER electrocatalysts derived from earth-abundant elements has become an urgent priority.<sup>8</sup> Transition metal (TM)-based oxides/phosphides have been regarded as the most promising OER electrocatalysts due to their unfilled 3d, low cost, and relatively high efficiency. However, a relatively large overpotential is still required by the OER, even when using TM-based electrocatalysts.<sup>8, 9</sup> This indicates that substantial improvements cannot be achieved solely through the design and regulation of electrocatalyst materials. To push beyond these intrinsic material limitations, the introduction of external stimuli has emerged as a promising strategy. Stimuli such as visible light, magnetic fields, and heating can provide additional driving forces that enhance charge transfer, accelerate reaction kinetics, and influence spin selection during catalytic processes.<sup>10, 11</sup> In particular, light-assisted catalysis (photoelectrocatalysis) can not only supply extra energy to lower activation barriers but also promote the generation of energetic charge carriers, thereby synergistically improving reaction efficiency.<sup>12, 13</sup> Similarly, magnetic and electric fields can modulate the spin states of intermediates and tune the electronic structure of active sites, which is especially relevant for reactions governed by spin selection rules.<sup>11</sup> Within this framework, the spin-sensitive nature of the OER is particularly noteworthy. Since OER involves the conversion of singlet-state reactants (OH<sup>−</sup> or H<sub>2</sub>O) into triplet-state O<sub>2</sub> molecules, spin selection becomes a critical factor in determining the overall reaction rate. Recent studies have highlighted that aligning the spin states of intermediates can significantly reduce kinetic barriers, thereby improving catalytic efficiency.<sup>14</sup> This has led to a growing interest in spintronic approaches to catalysis, where magnetic interactions are intentionally harnessed to optimize electrocatalytic performance.

<sup>a</sup> Department of Chemistry, Stockholm University, Stockholm, Sweden.<sup>b</sup> Department of Material Science and Engineering, Ångström Laboratory, Uppsala University, Uppsala, Sweden.

Supplementary Information available: Characterization of Ni–NiO and Ni–NiPO and electrochemical measurements. See DOI: 10.1039/x0xx00000x



One major problem with electrocatalysis, which is usually neglected, is the availability of fresh water for efficient splitting. As freshwater accessibility is low, the potential of direct use of seawater should be further explored as a source of clean energy. Due to the relatively small potential difference in between the OER reaction and oxidation of chlorine ions unwanted chlorine oxidation reactions may take place at the anode to form hypochlorite or hypochlorous acid.<sup>15, 16</sup> In addition, Cl<sup>-</sup> ions can accelerate electrode degradation through corrosion or by directly reacting with catalyst surfaces, forming unstable metal chloride-hydroxide layers. These processes diminish the catalytic performance. To address this issue, conventional approaches rely on freshwater purification, which itself requires substantial energy input, undermining the overall sustainability and economic feasibility of hydrogen production. Other than this, several strategies have been explored: operating in alkaline media to improve OER selectivity, designing chloride-resistant catalysts, and employing protective or selective membrane technologies. Hybrid approaches, such as integrating forward osmosis (FO) membranes or seawater reverse osmosis (SWRO) with electrolysis, can provide desalinated water directly to the electrolyzer, bypassing energy-intensive purification steps while mitigating chloride-related side reactions.<sup>17, 18</sup> Recent research highlights that combining material design with system-level solutions, including pH control, membrane architecture, and catalyst engineering, offers a practical pathway toward sustainable, large-scale seawater electrolysis for clean hydrogen production.<sup>19-21</sup> FO membranes can effectively desalinate seawater before it enters the electrolyzer, thereby mitigating Cl<sup>-</sup>-induced side reactions and corrosion. This hybrid FO-electrolysis approach not only bypasses the need for energy-intensive water purification steps but also improves the long-term stability and efficiency of large-scale electrolyzer setups, ultimately enhancing economic viability.

In this study, we explore a solution to tackle some of the problems outlined above. Two visions are integrated (i) an application viewpoint: electrocatalytic water splitting with catalysts responding to a magnetic field, and (ii) a technical outlook: a FO membrane coupled to a water electrolysis cell to directly use desalinated water for splitting. We report an efficient and robust nickel phosphide/phosphate catalyst to achieve stable artificial seawater oxidation with an overpotential of 310 mV in 1 M phosphate buffer at pH 8 under a magnetic field of 100 mT.

## Experimental

### Preparation of Ni-NiO electrode

Ni-NiO electrodes were fabricated on Ni-foam substrates using a hydrothermal method. Prior to fabrication, the Ni-foam was first ultra-sonicated in deionised water for 10 min followed by acetone for 10 min. For the synthesis of NiO, 2 mmol Ni(NO<sub>3</sub>)<sub>2</sub>•6H<sub>2</sub>O (Merck, 97%), 20 mmol CO(NH<sub>2</sub>)<sub>2</sub> (Merck) and 0.5 mmol [N(CH<sub>3</sub>)<sub>3</sub>]Br (CTAB) (Merck, ≥98%) in 20 mL of deionised water, followed by ultrasonic treatment for 30 minutes. The solution was then transferred to a 50 mL Teflon-

lined autoclave containing Ni-foam and heated at 120 °C for 6 h. A precipitate then formed on the Ni-foam, which was further calcined at 450 °C for 2 h to obtain nanostructured NiO deposited on the Ni-foam (Ni-NiO) electrodes.<sup>22</sup>

### Preparation of Ni-NiPO electrode

For the phosphidation step, 0.2 g NaH<sub>2</sub>PO<sub>2</sub>•H<sub>2</sub>O (≥99%, Merck) was used in a furnace with an upstream Ar flow at 300 °C for 2h to convert nickel oxide to phosphides and form a Ni-NiPO electrode. During heat treatment, NaH<sub>2</sub>PO<sub>2</sub>•H<sub>2</sub>O releases PH<sub>3</sub>, which acts as a phosphorus source that reacts with the oxide and hydroxide precursors.<sup>23, 24</sup>

### Material Characterization

Powder X-ray diffraction (PXRD) data were obtained using a Bruker D8-Discover X-ray diffractometer with Cu K<sub>α</sub> radiation to identify the crystalline phases in the samples. The morphology of the catalyst materials on the electrodes were characterised using a field-emission scanning electron microscope (FE-SEM) JSM-7000F (JEOL) and transmission electron microscope (TEM) with JEM-2100F (JEOL). The elemental composition and distribution were investigated with energy dispersive X-ray spectroscopy (EDS) attached to JSM-IT800 (JEOL). High Angle Annular Dark Field-Scanning Transmission Electron Microscopy (HAADF-STEM) images and Energy Dispersive X-ray Spectroscopy (EDS) elemental mapping were obtained on a Thermo Fisher Scientific Themis Z operating at 300 kV equipped with a SuperX EDS detector. X-ray photoelectron spectroscopy (XPS) (Phi Quantra II) was carried out to analyse the chemical composition and valence states of the constituent elements in the samples. The spectrometer was equipped with an Al K<sub>α</sub> source and operated at 15 kV with a total power of 50 W. A pass energy of 224 eV was used to measure the survey spectra, while a pass energy of 55 eV was used to measure high-resolution XPS spectra. All XPS spectra were calibrated with C 1s high-resolution spectra, and the backgrounds were removed using the Shirley method. The binding energies for the Ni 2p high resolution spectra (2p<sub>1/2</sub> and 2p<sub>3/2</sub>), the O 1s spectra and P 2p are in accordance with the reported studies.<sup>25-28</sup>

The UV-visible absorption spectra of the resulting solutions were recorded using an Agilent Cary 5000 UV/Vis/NIR spectrophotometer. Fluorescence spectroscopy was performed using a Varian Cary Eclipse Fluorescence spectrophotometer. The phosphate concentration in the artificial seawater, chloride concentration in the electrolyte and hypochlorite concentration formed due to chloride oxidation in the electrolyte were determined using a method reported by Veroneau et al.<sup>15, 29</sup>

### Electrochemical Measurements

The electrochemical properties were measured at room temperature in a standard three-electrode set-up using an SP-50e potentiostat (Biologic). The catalyst electrodes were used as working electrodes. Ag/AgCl and platinum electrodes were used as reference and counter electrodes, respectively. The electrolytes for the OER analysis were 1 M phosphate buffer with different pH (pH 6, 7 and 8). The Linear sweep voltammetry (LSV) curves were collected at a scan rate of 5 mV s<sup>-1</sup>,



respectively. The iR drop for the LSV curves was directly compensated by the potentiostat at 85%, and the compensated resistance was about 2 to 3  $\Omega$ . LSV curves were obtained after 50 cycles of CV to activate the catalysts. The potentiostatic electrical impedance spectroscopy (PEIS) was conducted at a constant potential in the frequency range of 200 kHz to 100 mHz, and fitted using Zfit software. The potentials recorded from electrochemical tests were calibrated to the reversible hydrogen electrode (RHE) by using the equation:  $E_{RHE} = E_{Ag/AgCl} +$

$0.059 \times \text{pH}$ . The overpotential of OER ( $\eta_{OER}$ ) was calculated using the equation:  $\eta_{OER} = E_{RHE} - 1.23$ . The  $\eta_{OER}$  was calculated at the current density of 10  $\text{mA}/\text{cm}^2$  for all the experiments. The electrochemical active surface area (ECSA) of an electrode was estimated by using the equation:  $\text{ECSA} = C_{dl}/C_s$ , where  $C_{dl}$  is the electrochemical double-layer capacitance and is calculated by measuring the non-Faradaic capacitive current from the scan-rate dependent cyclic voltammetry (CV) curves.  $C_s$  is the specific capacitance for a flat surface; the reported  $C_s$  is generally 30  $\mu\text{F}$

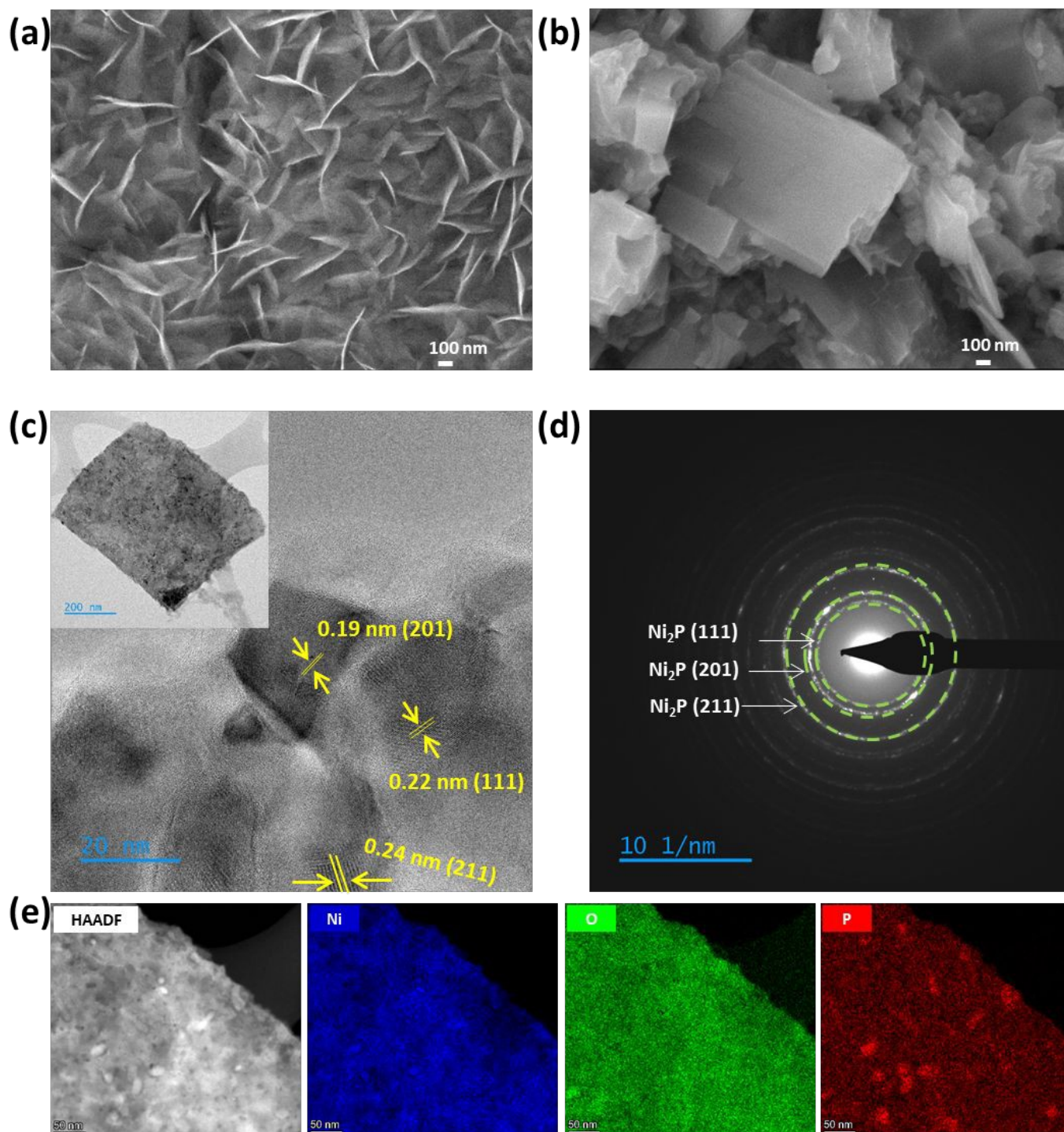


**Figure 1.** SEM images of (a) Ni-NiO, (b) Ni-NiPO. (c) HRTEM images of Ni-NiPO. (d) SAED patterns of Ni-NiPO. (e) HAADF-STEM image and EDS mapping of Ni-NiPO.



$\text{cm}^{-2}$ . The ECSA was used to normalise current and  $C_{dl}$ . The stability of the catalysts was observed by conducting chronoamperometry and chronopotentiometry for 36–48 h. Prior to electrochemical measurements, the electrolyte was purged with  $\text{N}_2$  gas to remove dissolved oxygen present in the electrolyte.

### Preparation of a forward osmosis membrane coupled water splitting (FOWS) cell

The forward osmosis cell (FOWS) was constructed by connecting a 50 ml plastic centrifuge tube containing the electrolyte consisting of 1 M phosphate buffer (pH 6, 7 and 8), in which the electrolysis takes place with a three-electrode configuration (WE, RE and CE) and an external solution of artificial seawater containing 0.5 M NaCl solution. The two solutions were in contact via a commercially available forward osmosis membrane (FO) made of cellulose triacetate from STERLITECH (FTSH2O Flat Sheet Membrane). The membrane has limited functionality at pH values higher than 7.

### Magneto-electrochemical measurements

Neodymium-based permanent disk magnets of radius 25 mm and thickness 10 mm were placed outside the electrocatalytic setup. Two such magnets were placed opposite to each other on the circumference of the electrocatalytic cells, resulting in a magnetic field of 100 mT at the centre of the cell. The magnetic field was measured using a Gauss meter (ZMST-5 Digital Tesla meter). The magnetic field was applied perpendicular to the electric field.

## Results and discussion

### Morphology and Phase Composition

Nanoflakes of nickel oxide/hydroxide were synthesised on Ni-foam using a hydrothermal technique (hereafter named Ni-NiO), see Figure 1a (Figure S1, S2). Subsequently, the nickel oxide/hydroxide were partially converted into nickel phosphides and phosphates (hereafter named Ni-NiPO) during phosphidation in a tube furnace at elevated temperature. The morphology transformed from nanoflakes to layered nanoparticles (Figure 1b). The presence and homogeneous distribution of Ni, P, and O are confirmed from EDS mapping and from EDS spectra (Figure S3, S4).

The Ni-NiPO sample was further investigated by use of transmission electron microscopy (TEM). Low-resolution TEM images show a similar morphology to what is observed in SEM (Figure 1c: inset). High-resolution TEM reveals interplanar distances of 0.19, 0.22 and 0.24 nm, which can be attributed to the (201), (111), and (211) planes of the  $\text{Ni}_2\text{P}$  phase (Figure 1c). The SAED pattern shows (111), (201), and (211) planes of the  $\text{Ni}_2\text{P}$  phase (Figure 1d), in agreement with previous studies of  $\text{Ni}_2\text{P}$ .<sup>30, 31</sup> High-angle annular dark-field scanning TEM (HAADF-STEM) clearly shows formation of nickel phosphide nanoflakes (Figure 1e). Energy-dispersive X-ray spectrometry mapping shows a relatively homogeneous distribution of oxygen, indicating the presence of phosphates.

Powder X-ray diffraction (PXRD) pattern of Ni-NiO agree with the diffraction files of NiO (PDF 47-1049) and  $\beta\text{-Ni}(\text{OH})_2$  (PDF 01-0117), see Figure S5.<sup>32, 33</sup> The diffraction peaks at  $2\theta = 20.6$ , 28.6, 37.6, and 63.3 can be indexed to the (001), (100), (101), and (111) planes of NiO and the  $2\theta = 37.6$ , 43.7, and 63.3 can be indexed to the (101), (200), and (111) planes of  $\beta\text{-Ni}(\text{OH})_2$ , respectively along with the  $2\theta$  peaks of Ni-foam at 44.5 (111) and 51.9 (200).<sup>25</sup>

After phosphidation, the PXRD pattern of Ni-NiPO shows  $\text{Ni}_2\text{P}$  (PDF 04-003-1863) with the diffraction peaks at  $2\theta = 40.9$ , 45.6, 47.6, 52.6, 53.1, and 59.3 indexed to (111), (201), (210), (110), (300), and (211).<sup>34</sup> Also, the presence of nickel phosphates is observed in the Ni-NiPO catalyst. Several broad diffraction peaks match with the phosphate phases of  $\text{Ni}_2(\text{PO}_3)_4$  (PDF 01-076-1557),  $\text{Ni}_2\text{P}_2\text{O}_7$  (PDF 04-014-1816) and  $\text{Ni}_3(\text{PO}_4)_3$  (PDF 00-035-0987).<sup>35</sup> Thus, a partial conversion of oxides and hydroxides to phosphates occurs along with the formation of nickel phosphide ( $\text{Ni}_2\text{P}$ ) during phosphidation, see Figure 2a.

Further, from Raman spectroscopy, it is observed that in Ni-NiO, four Raman scattering peaks are present at 510, 742, 1085, and 1490  $\text{cm}^{-1}$ , that can be ascribed to the first-order longitudinal optical (LO1) phonon mode of the Ni–O lattice vibration, the second-order transverse (TO2), the second-order longitudinal optical (LO2) phonon modes, and the two-magnon (2 M) mode of the NiO, respectively (Figure S6a) in accordance with the peak assignments by Terlemezoglu et al.<sup>36</sup> Only non-stoichiometric NiO shows LO1 mode indicating the presence of defects, such as nickel vacancies. Raman spectra of crystalline  $\text{Ni}_2\text{P}$  are often weak or silent in the typical 100–1000  $\text{cm}^{-1}$  range because Ni–P modes couple poorly to Raman scattering. Instead, the peaks observed usually correspond to oxide species or their electrochemical transformations.<sup>37</sup> In addition to  $\text{Ni}_2\text{P}$ , also weak P–O–P (799  $\text{cm}^{-1}$ ) and P–O (1159  $\text{cm}^{-1}$ ) peaks are observed in the Ni-NiPO electrocatalyst, confirming presence of phosphates (Figure S6b).<sup>35</sup>

### XPS Characterisation

The surface oxidation states and electronic structure of the catalysts were analysed using X-ray photoelectron spectroscopy (XPS). All XPS spectra were calibrated using C 1s high-resolution spectra, and the backgrounds were removed using the Shirley method. As shown in Figure S7, the survey spectrum of Ni-NiO shows Ni 2p and O 1s, and for Ni-NiPO, also P 2p is observed. The Ni 2p high-resolution spectra for Ni-NiO are well-fitted with two spin-orbit doublets,  $2p_{1/2}$  (872 eV) and  $2p_{3/2}$  (854 eV), considering the 2:1 area proportion for the spin-split to  $2p_{3/2}$  and  $2p_{1/2}$ , as well as shakeup satellites (860.6 and 879.6 eV), see Figure 2c. Both doublets are peak-fitted into the oxidation states of Ni; +3 for 855.4 and 873.2 eV; and +2 for 853.8 and 871.2 eV. Similarly, the O 1s spectra of the Ni-NiO precursor, in Figure 2d, can also be fitted to two species, which include metal-oxide-bound species (529.2 eV) (lattice oxygen:  $\text{O}_L$ ), and oxygen vacancies on the surface (530.8 eV) ( $\text{O}_V$ ). For Ni-NiO,  $\text{O}_L$  and  $\text{O}_V$



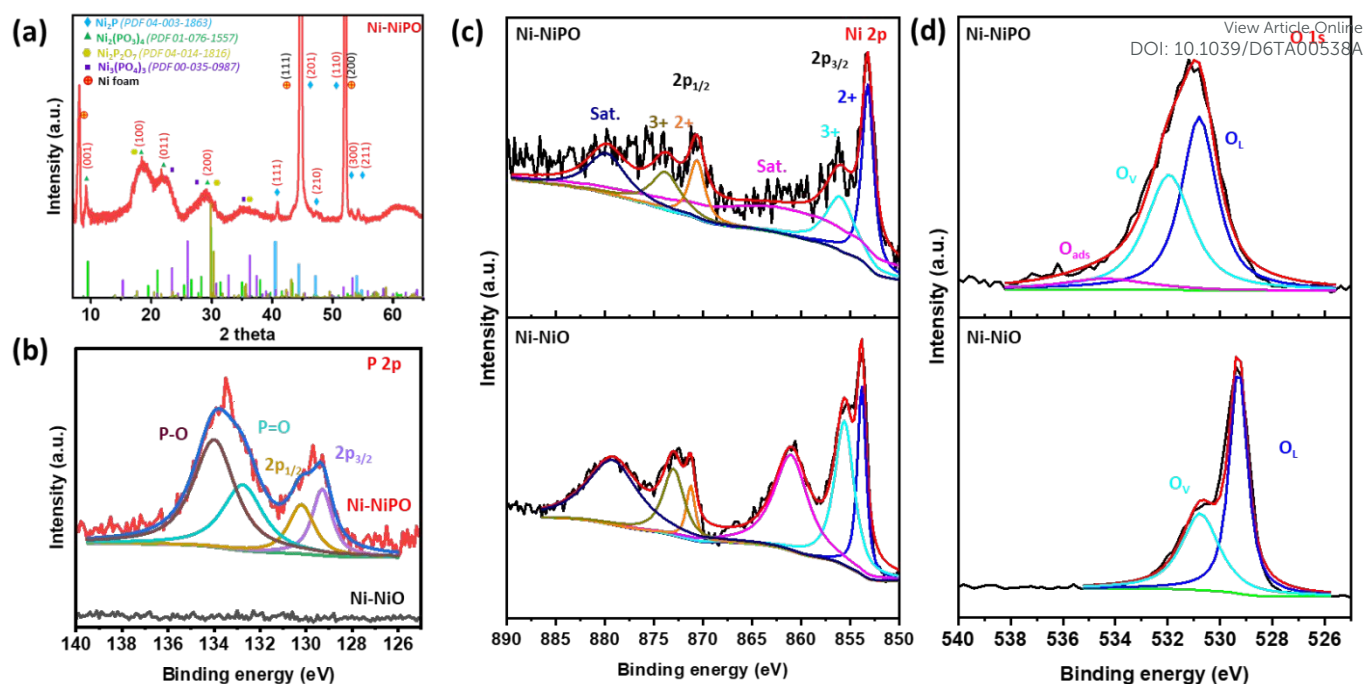


**Figure 2.** (a) Powder X-ray diffraction pattern for Ni-NiPO. Deconvoluted high-resolution XPS spectra of Ni-NiO and Ni-NiPO (b) P 2p, (c) Ni 2p, (d) O 1s.

are observed, confirming the formation of Ni-O bond and Ni-OH bond.

After thermal treatment with  $\text{NaH}_2\text{PO}_4 \cdot \text{H}_2\text{O}$ , the surface chemistry of the resulting Ni-NiPO is probed with XPS. The +3 state of both Ni  $2p_{3/2}$  and Ni  $2p_{1/2}$  comprises a higher binding energy shift (0.6 eV) in the peak position due to surface oxidation after phosphidation, with a partially charged  $\text{Ni}^{\delta+}$  ( $0 < \delta < 2$ ). The partially charged metal ions help to attain prompt electron transfer ability. It promotes more oxygen vacancies, which improve the -OH adsorption at the electrode surface. Along with this, the increased intensity of +2 states of both Ni  $2p_{3/2}$  and Ni  $2p_{1/2}$  proves the phosphide formation from the oxides. The O 1s core-level XPS spectra of Ni-NiPO can be divided into three peaks centred at 529.2 ( $\text{O}_L$ ), 532.0 ( $\text{O}_V$ ), and 534.8 eV, which can be attributed to adsorbed oxygen and hydroxide species as well as P-O components.<sup>38</sup> An increase in the binding energy of O 1s electrons typically indicates the presence of other atoms or groups (here, phosphorus) in the molecule and molecular geometry. Again, an increase in vacancy oxygen ( $\text{O}_V$ ) is observed for Ni-NiPO compared to Ni-NiO, which refers to the presence of oxygen vacancies in a material, particularly in catalysts. These vacancies are defects in the lattice structure of metal oxides or other compounds containing oxygen. They are formed during synthesis under elevated temperatures and reducing atmospheres and play a crucial role in the stability, diffusivity, and catalytic activity of the material. The P 2p region clearly represents two different environments around phosphorus (Figure 2b): metal phosphide (P  $2p_{3/2}$  = 129.2 eV and P  $2p_{1/2}$  = 130.2 eV) and oxidised phosphate species P=O (132.8 eV) and P-O (134 eV) on the surface. The binding energy of P 2p of Ni-NiPO is negatively shifted from that of elemental P (130.2 eV), which proposes a

partial negative charge ( $\delta^-$ ) on the P atom. The peak at 134 eV is attributed to an oxidised form of P atoms resulting from surface oxidation of the phosphide phase to phosphates.

### Electrocatalytic performance

#### Electrocatalytic OER in three-electrode setup in 1M phosphate buffer electrolyte

To evaluate the electrocatalytic activity, OER was first performed in an oxygen saturated 1 M phosphate buffer at pH 6, 7, and 8, using the catalyst Ni-NiPO. Linear sweep voltammetry (LSV) was performed with a conventional three-electrode setup followed by measurements in the forward osmosis cell (FOWS) (Figure 3a), using the same setup as in our previous work.<sup>39</sup> From the initial LSV measurements, the overpotentials were observed to be 950, 580, and 450 mV at pH 6, 7, and 8, respectively (Figure 3b). The lowest overpotential is thus observed at pH 8 as alkaline electrolytes provide stabilisation of key intermediates by the presence of hydroxide ions. The Tafel slopes, calculated from the LSV measurement, shows 133, 86 and 77 mV/dec for pH 6, 7, and 8, respectively, reflecting the improved charge-transfer kinetics (Figure S8).

#### Electrocatalytic OER with FOWS setup

The next step was to use the FOWS setup, as our aim is to utilize seawater for electrocatalytic water oxidation. The FOWS cell was equipped with a three-electrode setup, and the concentration of the electrolyte was chosen to compensate for the influx provided by the high surface area of the forward osmosis membrane. In the FOWS experiments, an external vessel containing 0.5 M NaCl solution (artificial seawater, 0.5 M NaCl = 3.5 wt% NaCl) was in contact with the electrochemical



cell containing the phosphate buffer solution via a forward osmosis membrane.<sup>39</sup> LSV measurements were carried out over time at three different pH levels (Figure 3c). It is observed that the overpotentials has increased after 1 and 2 h at pH 6 and 7, whereas at pH 8 the overpotential remains almost the same during 2h (Figure 3d, Table S1). The overpotential values are calculated after repeating the experiments three times. Along with the lowest overpotential, Ni-NiPO is least affected at pH 8. To understand the interfacial interaction, impedance spectroscopy was carried out in 1 M phosphate buffer at different pH levels. Nyquist plots for Ni-NiPO show that the decrease in  $\text{Re}(Z)$  happens rapidly with an increase in pH (Figure 3e). The charge-transfer resistance ( $R_{ct}$ ) is smallest at pH 8 (12.3 ohm) and highest at pH 6 (35.9 ohm). Also, from the Nyquist plot, the double-layer capacitance ( $C_{dl}$ ) was calculated for the electrolyte 1 M phosphate buffer (Table S2). The  $C_{dl}$  increases as the pH increases from pH 6 (0.8 mF) to pH 8 (1.0 mF). The  $C_{dl}$  was used to evaluate the electrochemically active surface area (ECSA) of Ni-NiPO, as  $C_{dl}$  is directly proportional to ECSA. To evaluate the stability, chronopotentiometry was also performed at 10 mA applied current. At pH 7 and 8, the potential reached up to 0.44 V and 0.52 V, respectively, with consistency for 48 hours (Figure 3f). But in the case of pH 6, the achieved potential is initially high (1.36 V) and not so stable over time, indicating corrosion of the Ni-electrode. The incorporation of a semipermeable FO membrane markedly suppresses the concentrations of chloride and its oxidation

products, thereby minimizing their accumulation on both anode and cathode surfaces. This improvement is primarily attributed to the effective rejection of  $\text{Cl}^-$  ions via forward osmosis, the reduced operational potential required for the OER, and the employment of sodium phosphate as the electrolyte, which serves as a superior promoter of OER relative to ClOR. Owing to its selective ion exclusion properties and minimal leaching through the FO membrane, sodium phosphate represents an optimal inner electrolyte for FOWS cells operated under near neutral conditions.

#### Electrocatalytic OER in artificial seawater + 1 M phosphate buffer

In a third setup, it was found that during electrolysis of artificial seawater (0.5 M NaCl) + 1 M phosphate buffer, the performance is not affected at pH 8 (Figure 4a). However, the stability of OER at pH 6 and 7 ceases after 3 and 9 hours, respectively. The overpotential for OER at pH 8 is much lower compared to at pH 6 and 7 and the stability was intact during the testing period of 48 hours. Since the overpotential at pH 8 is low, the risk for ClOR is also lower compared to at pH 6 and 7 where the overpotential is closer to the ClOR oxidation potential, which may disrupt a stable chronoamperometric behaviour due to corrosion of the catalyst. It is thus clear that the FO membrane plays a crucial role in the setup where the artificial seawater is separated from the phosphate buffer via the FO membrane by selectively transporting water molecules while effectively blocking the

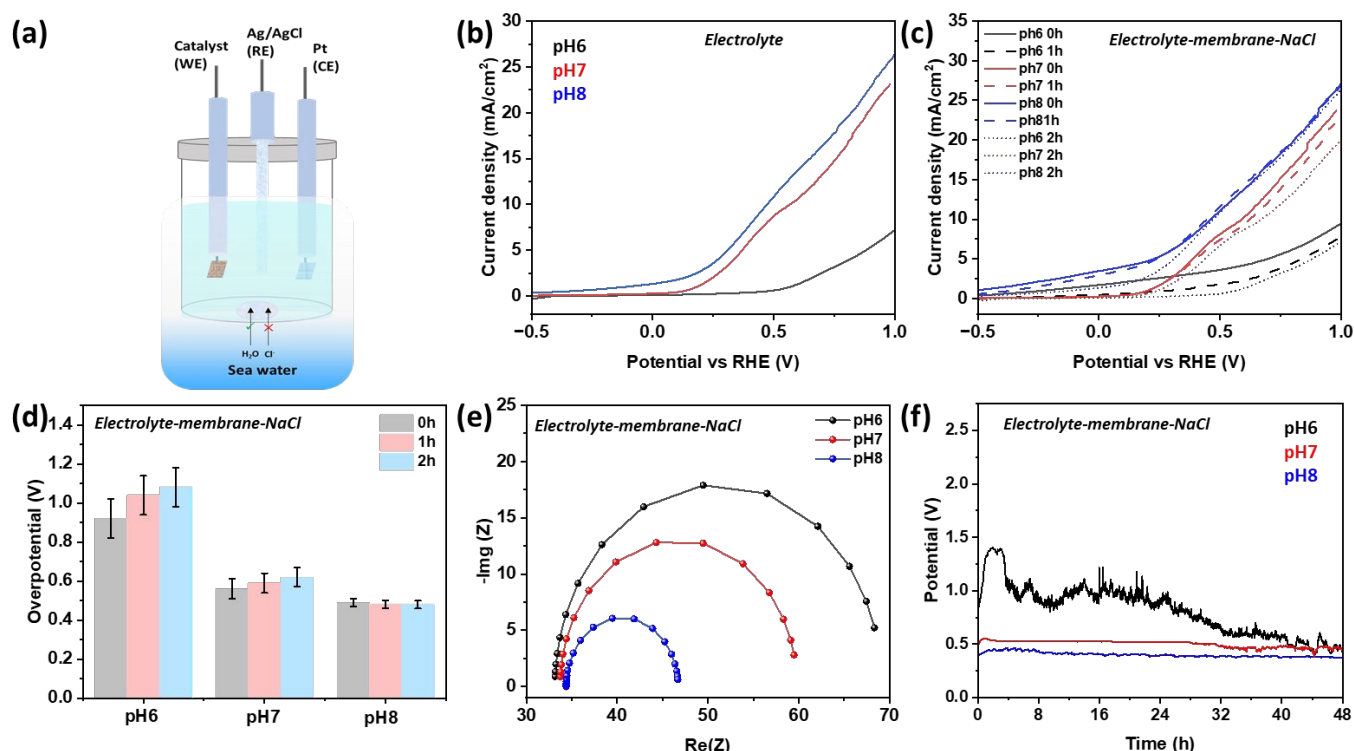


**Figure 3.** Electrochemical performance of the Ni-NiPO catalyst in 1 M phosphate buffer (pH 6, 7 and 8). (a) Schematic diagram of the FOWS setup. (b) Linear sweep voltammetry of Ni-NiPO with conventional three-electrode setup. (c) Linear sweep voltammetry after different contact times of the Ni-NiPO catalyst with the electrolyte using the FOWS setup. (d) Overpotential of the Ni-NiPO catalyst after different contact times in the FOWS setup. (e) Impedance spectroscopy: Nyquist plots of Ni-NiPO with FOWS setup. (f) Chronopotentiometry of Ni-NiPO with FOWS setup.



migration of chloride ions. This selective ion transport is important because it suppresses unwanted corrosion of the electrode surface, which otherwise occurs when electrodes are directly exposed to artificial seawater.<sup>16</sup>

#### Electrocatalytic OER in artificial seawater with FOWS setup in presence of magnetic field

Recently, we have established that the effect of a magnetic field ( $B = 100$  and  $200$  mT) can enhance the OER efficiency using mixed metal phosphides (NiCoP and NiCoFeP).<sup>40</sup> Inspired by those results, we applied a magnetic field of  $100$  mT in parallel with the electric field, also for the present catalyst in the FOWS cell for the electrocatalytic OER process, The LSVs were acquired after different times up to  $24$  h to evaluate the effect of an applied magnetic field ( $B = 100$  mT) at pH 6, 7 and 8 (Figure 4b, S9). It is observed that the overpotential is lowered in the presence of a magnetic field, and with time, the overpotential decreases for all three pH values used. The overpotential achieved after applying a magnetic field for  $24$  hours at pH 8 ( $310$  mV) is the lowest compared to pH 7 ( $390$  mV) and pH 6 ( $620$  mV) (Figure S10, Table S3). The differences with and without an applied magnetic field ( $100$  mT) in the FOWS setup were investigated, and the overpotential was measured after different times, see Figure 4c. With time, a lowering in overpotential is observed when a magnetic field is applied, while the overpotential increases with time without an applied magnetic field (Table S1, S3). The results indicate that it

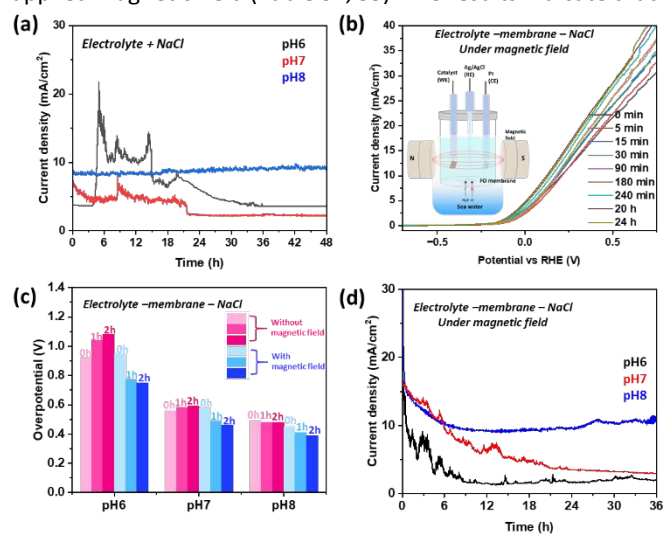


**Figure 4.** (a) Chronoamperometry for OER with Ni-NiPO catalyst in 1 M phosphate buffer +  $0.5$  M NaCl at pH 6, 7 and 8 without the FOWS setup. (b) Linear sweep voltammetry of Ni-NiPO in 1 M phosphate-buffer (pH 8) with FOWS setup under magnetic field with time interval (inset: Schematic diagram for the FOWS setup with magnetic field). (c) Comparison of overpotential of the Ni-NiPO catalyst in 1 M phosphate buffer (pH 6, 7 and 8) with different time interval ( $0, 1, 2$  h) with FOWS setup with (blue) and without (pink) magnetic field. (d) Chronoamperometry for OER with Ni-NiPO catalyst in 1 M phosphate buffer at pH 6, 7 and 8, under magnetic field ( $B = 100$  mT) with FOWS setup.

takes a relatively long time for the magnetic domains to align when a magnetic field is applied. Tafel slopes are calculated from the LSVs in Figure 4b. They show a gradual decrease from  $80$  to  $42$  mV/dec, explaining the improvement in the kinetics in presence of magnetic field (Figure S11). The Impedance spectroscopy was performed at pH 8 in a FOWS setup under magnetic field. From the Nyquist plot, it is observed that the  $R_{ct}$  decreases with time in presence of magnetic field,  $B = 100$  mT (Figure S12, Table S4). The  $R_{ct}$  decreases to  $11$  ohm from  $14.9$  ohm after  $15$  minutes of magnetic field and reaches  $7.7$  ohm after  $60$  minutes. It reflects the influence of magnetic field in enhancing the conductivity during the electrocatalytic OER. As an external stimulus, a magnetic field enhanced the efficiency of electrocatalysis and the water splitting process can be kinetically enhanced. The electrocatalytic effects associated with the applied magnetic field are explained by the magneto-hydrodynamic effect, spin selection, and magneto-resistance.<sup>11, 41-44</sup> This occurs due to the (i) magneto-hydrodynamic effect; as the magnetic field is placed perpendicularly to the electric field, the Lorentz force creates and removes gas bubbles at the electrode surface, (ii) higher conductivity as the magnetic domains of the catalyst gets aligned in presence of a magnetic field to reduce the resistivity (observed in the trend of charge-transfer resistance) to enhance the mass-transport of the reaction, and (iii) spin-modification for the spin-dependant reactions like OER, the magnetic field helps to align the spin of the oxygen radical to initiate O-O bond easily.<sup>14</sup> These are the responsible reasons to improve the catalytic activity in presence of magnetic field.

To evaluate the stability of the Ni-NiPO catalyst when applying an FOWS setup and magnetic field, chronoamperometry was performed (Figure 4d). In the electrolyte with pH 8, the current density is observed to be stable during a  $36$  h experiment at  $10$  mA/cm<sup>2</sup>, while at pH 6 and pH 7, the current density decreases with time. Further, the stability was studied for  $6$  days in  $1$  M phosphate buffer pH 6, 7 and 8, showing a stable performance (Figure S13). As it observed that the current density is very stable at pH 8, while the current density is unstable for pH 6 and 7.

#### Electrocatalytic OER in 1 M phosphate buffer in presence of magnetic field

Magneto-electrocatalytic OER in  $1$  M phosphate buffer (pH 6, 7 and 8) was performed also without the FOWS setup, (Figure S14). The change in overpotential is then similar to the overpotential drop while performing in saline water with the FOWS setup under a magnetic field ( $B = 100$  mT) (Table S5). This implies that FOWS helps to achieve a similar performance as when there is no contact with salt water.

The leaching of  $Cl^-$  and  $Na^+$  ions into the electrolysis cell and leakage of phosphate out from the cell through the FO membrane is crucial during long-term runs. To have a better understanding of these properties, spectrophotometric analysis was performed to determine any probable leakages, following previous studies.<sup>15, 39</sup> The concentrations of chloride ions (Figure S15) and their oxidation products (Figure S16) were measured in the inner electrolyte chamber through



fluorescence spectroscopy and UV-Visible spectroscopy, respectively. Along with that, the concentration of phosphate leaching through the FO membrane in the outer electrolyte was measured with UV-Visible spectroscopy (Figure S17). As observed, the phosphate leaching is around 0.1 mmol after 48 h at pH 6, which is around 0.5% of the content in the electrolyte. However, at pH 7 and pH 8, the phosphate leaching is around 1.1 mmol (5.5% of the electrolyte) and 1.2 mmol (6% of the electrolyte), respectively, after 48 h. This is mainly due to the operating limitations of the FO membrane. The amount of chloride in the electrolyte was ca 42 mmol at pH 6 (8.4% of the artificial seawater), 51 mmol at pH 7 (10.2% of the artificial seawater) and 58 mmol at pH 8 (10.4% of the artificial seawater) after 48 h of continuous operation. The increase in chloride concentration with increasing pH is also due to the pH dependent operational limitations of the FO membrane. However, these influxes are ~10% of the of the chloride ions from the artificial seawater and the electrocatalysts are thus less exposed to chloride ions with an FO membrane as compared to direct seawater splitting. The chloride oxidation products, such as HOCl/OCl<sup>-</sup>, produced during the continuous operation were evaluated to be ca 0.21 mmol at pH 6, 0.17 mmol at pH 7, and 0.14 mmol at pH 8. With increasing pH, the oxidation products decrease as the overpotential needed for water oxidation also decreases.

#### Characterization after electrocatalysis experiments

Characterization by use of SEM, XRD, and XPS of Ni-NiPO were performed after chronoamperometry for 48 hours in 1 M phosphate buffer electrolyte at different pH values. SEM shows that the morphology of Ni-NiPO changes after OER in 1 M phosphate buffer (pH 6), see Figure S18. In contrast, the morphology of the same catalyst is fairly intact after reaction at pH 8. XRD also clearly shows that after reaction at pH 6, the phosphide phase has mainly been converted to oxides. However, Ni-NiPO that reacts at pH 8 shows low oxidation, and the Ni<sub>2</sub>P phase is still present, see Figure S19. XPS was performed after OER, see Figures S20-23, and an increase in the binding energy of Ni 2p is observed due to the presence of oxygen on the surface of the material. The high-resolution P 2p spectra lack the P 2p<sub>1/2</sub> and P 2p<sub>3/2</sub> peaks for the catalyst after use at pH 6 and pH 7, while they are present at pH 8. This indicates the stability of Ni-NiPO after 48 hours of electrocatalysis at pH 8, as P 2p HRXPS shows intact P 2p<sub>1/2</sub> and P 2p<sub>3/2</sub> peaks together with P-O and P=O as P 2p. However, in the case of pH 6 and 7, the absence of P 2p<sub>1/2</sub> and P 2p<sub>3/2</sub> supports the chronoamperometric data in Figure 4d, where the stability of the catalyst at pH 8 is superior to that at pH 6 and 7 due to degradation of the phosphide phase during electrocatalysis. Along with this, the high-resolution deconvoluted Ni 2p spectra show a disappearance of the +2 state peak after use at both pH 6 and pH 7, confirming oxidation of the catalyst. However, at pH 8, the +2 states of Ni 2p coexist with the +3 states after OER, indicating a better stability of the catalyst. After electrochemistry, the O 1s peak appeared at 535 eV at pH 8, indicating the presence of strongly bound physisorbed oxygen species.

## Conclusions

View Article Online

DOI: 10.1039/D6TA00538A

Ni-based phosphide catalysts synthesised on Ni foam and integrated with forward osmosis membranes are shown to be a promising method for direct seawater splitting. Powder X-ray diffraction and X-ray photoelectron spectroscopy verify the formation of nickel phosphide and phosphate phases from an oxide precursor. However, the conversion is not complete and oxide and hydroxide phases also remain after phosphidation. The electrocatalytic cell is designed with a chloride-ion-selective forward osmosis membrane to improve performance and durability by preventing chlorine oxidation and electrode corrosion.

The forward osmosis membrane effectively suppresses chloride ion transport while enabling rapid water transfer, reducing electrode corrosion. The best performance was achieved at pH 8, where the FO membrane offered superior stability over 48 h and high selectivity for OER compared to CIOR in saline environments. In addition, the application of an external magnetic field (~100 mT) improves the oxygen evolution reaction by lowering the overpotential from 0.45 V to 0.31 V and promoting the reaction kinetics.

After 48 hours of continuous operation, phosphate leaching is approximately 1.2 mmol (6% of the inner electrolyte) at pH 8, and chloride accumulation reached approximately 85 mmol. The observed increase in chloride accumulation with rising pH can be attributed to the pH-dependent operating limitations of the FO membrane. Despite this, the chloride influx remains around 10% of the total chloride ion concentration in the artificial seawater (outer electrolyte). By mitigating electrode degradation and reducing the chlorine evolution reaction (CIOR) as well as lowering the required overpotential through the synergistic application of magnetic and electric fields, this work presents a compelling strategy for the development of efficient and sustainable seawater-splitting systems.

Furthermore, the FOWS cell with the nickel phosphide/phosphate/oxide catalyst outperforms most recently reported electrocatalysts for OER in neutral seawater (see Table S6). Continued research with different electrolytes and buffer systems may further improve performance by increasing ion selectivity and reducing electrolyte transfer. In addition to the performance and durability of the anode materials, the stability and catalytic activity of the cathode are equally important for efficient water splitting. It is worth noting that the use of an FOWS cell reduces precipitation on the cathode surface, as demonstrated in the study by Veroneau et al.<sup>15</sup> Furthermore, the efficiency of the water oxidation process can be improved by utilizing a superior membrane with better durability across the pH scale.

## Author contributions

The manuscript was written through contributions of all authors. All authors have given approval to the final version of the manuscript. JS, TKS and MJ have designed the project and performed the synthesis, phase characterization and electrochemical



measurements. JM and GSA have performed the XPS characterization.

## Conflicts of interest

There are no conflicts to declare.

## Data availability

The data that support the findings of this study are included in the article and its supplementary information (SI).

## Acknowledgements

The authors acknowledge the use of the EM facilities and the assistance of Dr. Anumol Ashok at the Electron Microscopy Center at Stockholm University as well as Dr. José Montero for assistance with collecting the XPS data.

## References

- B. H. R. Suryanto, Y. Wang, R. K. Hocking, W. Adamson, C. Zhao, *Nat. Commun.*, 2019, **10** (1), 1–10. <https://doi.org/10.1038/s41467-019-13415-8>.
- C. Mohapatra, S. Ayushi, R. Sarma, A. Sharma, S. S. Meena, P. M. Pataniya, C.K. Sumesh, N.K. Prasad, *Ceramics Int.*, 2025, **51**, 52649–52661. <https://doi.org/10.1016/j.ceramint.2025.09.022>.
- H. K. Thakkar, K. H. Modi, K. K. Joshi, G. Bhadu, S. Siraj, P. Sahatiya, P. M. Pataniya, C. K. Sumesh, *ACS Sustainable Chem. Eng.*, 2024, **12**, 8340–8352. <https://doi.org/10.1021/acssuschemeng.4c00591>.
- S. V. Chauhan, K. K. Joshi, P. M. Pataniya, P. Sahatiya, G. Bhadu, C.K. Sumesh, *Renewable Energy*, 2025, **24**, 122370. <https://doi.org/10.1016/j.renene.2025.122370>.
- N. A. Trivedi, P. J. Sharma, K. K. Joshi, V. Patel, C.K. Sumesh, P. M. Pataniya, *International Journal of Hydrogen Energy*, 2024, **61**, 1212–1219. <https://doi.org/10.1016/j.ijhydene.2024.03.050>.
- R. D. L. Smith, M. S. Prévot, R. D. Fagan, S. Trudel, C. P. Berlinguette, *J. Am. Chem. Soc.*, 2013, **135** (31), 11580–11586. <https://doi.org/10.1021/ja403102j>.
- S. Kundu, B. Malik, D. K. Pattanayak, V. K. Pillai, *ACS Appl. Mater. Interfaces*, 2017, **9** (44), 38409–38418. <https://doi.org/10.1021/acsaem.7b09601>.
- M. J. Craig, G. Coulter, E. Dolan, J. Soriano-López, E. Mates-Torres, W. Schmitt, M. García-Melchor, *Nat. Commun.*, 2019, **10** (1), 1–9. <https://doi.org/10.1038/s41467-019-12994-w>.
- J. Wang, L. Gan, W. Zhang, Y. Peng, H. Yu, Q. Yan, X. Xia, X. Wang, *Sci. Adv.*, 2018, **4** (3), 1–9. <https://doi.org/10.1126/sciadv.aap7970>.
- C. Ding, J. Shi, Z. Wang, C. Li, *ACS Catal.*, 2017, **7** (1), 675–688. <https://doi.org/10.1021/acscatal.6b03107>.
- F. A. Garcés-pineda, M. Blasco-ahicart, D. Nieto-castro, N. López, J. R. Galán-mascarós, *Nat. Energy*, 2019, **4** (June), 519–525. <https://doi.org/10.1038/s41560-019-0404-4>.
- J. Yu, J. González-Cobos, F. Dappozze, P. Vernoux, A. Caravaca, C. Guillard, *Green Chem.*, 2024, **26**, 1682–1709. <https://doi.org/10.1039/d3gc03371f>.
- D. Liu, X. Wan, T. Kong, W. Hanc, Y. Xiong, *J. Mater. Chem. A*, 2022, **10**, 5878–5889. <https://doi.org/10.1039/d1ta08252c>.
- C. A. Mesa, F. A. Garcés-Pineda, M. García-Tecedor, J. Yu, B. Khezri, S. Plana-Ruiz, B. López, R. Iturbe, N. López, S. Gimenez, *APL Energy*, 2024, **2** (1), 016106. <https://doi.org/10.1063/5.0179761>. DOI: 10.1039/D6TA00538A
- S. S. Veroneau, A. C. Hartnett, A. E. Thorarinsdottir, D. G. Nocera, *ACS Appl. Energy Mater.*, 2022, **5** (2), 1403–1408. <https://doi.org/10.1021/acsaem.1c03998>.
- S. Dresp, F. Dionigi, M. Klingenhof, P. Strasser, *ACS Energy Lett.*, 2019, **4** (4), 933–942. <https://doi.org/10.1021/acscenergylett.9b00220>.
- G. S. Cassol, C. Shang, A. K. An, *Nat. Commun.*, 2024, **15**, 2617. <https://doi.org/10.1038/s41467-024-46964-8>.
- J. Guo, Y. Zheng, Z. Hu, *Nat. Energy*, 2023, **8**, 264–272. <https://doi.org/10.1038/s41560-023-01195-x>.
- W. Yu, Z. Zhang, F. Luo, *Nat. Commun.*, 2024, **15**, 10220. <https://doi.org/10.1038/s41467-024-54514-5>.
- M. A. Blommaert, D. Aili, R. A. Tufa, Q. Li, W. A. Smith, D. A. Vermaas, *ACS Energy Lett.*, 2021, **6** (7), 2539–2548. <https://doi.org/10.1021/acscenergylett.1c00618>.
- G. Liu, Y. Xu, T. Yang, L. Jiang, *Nano Materials Science*, 2023, **5**, 101–116. <https://doi.org/10.1016/j.nanoms.2020.12.003>.
- T. H. Ko, K. Devarayan, M. K. Seo, H. Y. Kim, B. S. Kim, *Sci. Rep.*, 2016, **6**, 1–9. <https://doi.org/10.1038/srep20313>.
- L. Ji, J. Wang, X. Teng, T. J. Meyer, Z. Chen, *ACS Catal.*, 2020, **10** (1), 412–419. <https://doi.org/10.1021/acscatal.9b03623>.
- J. Li, J. Li, X. Zhou, Z. Xia, W. Gao, Y. Ma, Y. Qu, *ACS Appl. Mater. Interfaces*, 2016, **8** (17), 10826–10834. <https://doi.org/10.1021/acsaem.6b00731>.
- X. Hu, X. Tian, Y. W. Lin, Z. Wang, *RSC Adv.*, 2019, **9** (54), 31563–31571. <https://doi.org/10.1039/c9ra07258f>.
- M. Cheng, H. Fan, Y. Song, Y. Cui, R. Wang, *Dalt. Trans.*, 2017, **46** (28), 9201–9209. <https://doi.org/10.1039/c7dt01289f>.
- J. T. Ren, L. Chen, H. Y. Wang, W. W. Tian, X. L. Song, Q. H. Kong, Z. Y. Yuan, *ACS Catal.*, 2023, **13** (14), 9792–9805. <https://doi.org/10.1021/acscatal.3c01885>.
- K. H. Modi, P. M. Pataniya, S. Siraj, P. Sahatiya, V. Patel, C. K. Sumesh, *Journal of Energy Storage*, 2023, **63**, 107040. <https://doi.org/10.1016/j.ceramint.2025.09.022>.
- S. S. Veroneau, D. G. Nocera, *Proc. Natl. Acad. Sci. U. S. A.*, 2021, **118**, e2024855118. <https://doi.org/10.1073/pnas.2024855118>.
- C. Du, L. Yang, F. Yang, G. Cheng, W. Luo, *ACS Catal.*, 2017, **7** (6), 4131–4137. <https://doi.org/10.1021/acscatal.7b00662>.
- J. Bian, C. Sun, *Adv. Energy Sustain. Res.*, 2021, **2** (6), 1–8. <https://doi.org/10.1002/aesr.202000104>.
- S. Rakshit, S. Ghosh, S. Chall, S. S. Mati, S. P. Moulik, S. C. Bhattacharya, *RSC Adv.*, 2013, **3** (42), 19348–19356. <https://doi.org/10.1039/c3ra42628a>.
- Z. Wu, X. L. Huang, Z. L. Wang, J. J. Xu, H. G. Wang, X. B. Zhang, *Sci. Rep.*, 2014, **4**, 3669. <https://doi.org/10.1038/srep03669>.
- L. Feng, H. Vruble, M. Bensimon, X. Hu, *Phys. Chem. Chem. Phys.*, 2014, **16** (13), 5917–5921. <https://doi.org/10.1039/c4cp00482e>.
- H. Aziam, S. Indris, M. Knapp, H. Ehrenberg, I. Saadoune, *ChemElectroChem*, 2020, **7**, 3866–3873. <https://doi.org/10.1002/celec.202001065>.
- M. Terlemezoglu, O. Surucu, M. Isik, N. M. Gasanly, M. Parlak, *Appl. Phys. A Mater. Sci. Process.*, 2022, **128** (1), 1–6. <https://doi.org/10.1007/s00339-021-05197-y>.
- J. Li, C. Xu, X. Li, Z. Su, *J. Phys. Conf. Ser.*, 2021, **1759** (1), 012012. <https://doi.org/10.1088/1742-6596/1759/1/012012>.
- M. Manikanta Kumar, R. Singh, C. R. Raj, *Chem. - An Asian J.*, 2024, **19** (23). <https://doi.org/10.1002/asia.202400684>.
- T. K. Sahu, J. Saha, A. Anil, G. Salazar-Alvarez, M. Johnsson, *ACS Appl. Energy Mater.*, 2024, **7** (10), 4445–4453. <https://doi.org/10.1021/acsaem.4c00386>.
- J. Saha, T. K. Sahu, J. Montero, A. Rydh, G. Salazar Alvarez, M. Johnsson, *ACS Appl. Energy Mater.*, 2025, **8** (15), 10868–10880. <https://doi.org/10.1021/acsaem.5c00746>.



## ARTICLE

Journal Name

- 41 Fahidy, T. Z. Hydrodynamic Models in Magneto-electrolysis. *Electrochim. Acta*, 1973, **18** (8), 607–614. [https://doi.org/10.1016/0013-4686\(73\)85026-1](https://doi.org/10.1016/0013-4686(73)85026-1).
- 42 L. Elias, A. C. Hegde, *Electrocatalysis*, 2017, **8** (4), 375–382. <https://doi.org/10.1007/s12678-017-0382-x>.
- 43 O. Devos, O. Aaboubi, J. P. Chopart, A. Olivier, C. Gabrielli, B. Tribollet, *J. Phys. Chem. A*, 2000, **104** (7), 1544–1548. <https://doi.org/10.1021/jp993696v>.
- 44 Y. Zhang, C. Liang, J. Wu, H. Liu, B. Zhang, Z. Jiang, S. Li, P. Xu, *ACS Appl. Energy Mater.*, 2020, **3** (11), 10303–10316. <https://doi.org/10.1021/acsaem.0c02104>.

View Article Online  
DOI: 10.1039/D6TA00538A

Journal of Materials Chemistry A Accepted Manuscript

Open Access Article. Published on 16 March 2026. Downloaded on 4/7/2026 7:51:07 AM.  
This article is licensed under a Creative Commons Attribution 3.0 Unported Licence.



**Data Availability Statement**

View Article Online  
DOI: 10.1039/D6TA00538A

Primary experimental data used in the study is available upon request to the corresponding author. That is e.g. experimental data from the characterization methods used.

Best regards

Mats

